

The role of low-level terrain-induced jets in rainfall variability in Tigris-Euphrates Headwaters

Amin K. Dezfuli^{*1,2} (amin.dezfuli@nasa.gov)

Benjamin F. Zaitchik³

Hamada S. Badr³

Jason Evans⁴

Christa D. Peters-Lidard¹

*Corresponding author

¹ NASA Goddard Space Flight Center

² Universities Space Research Association

³ Department of Earth and Planetary Sciences, Johns Hopkins University

⁴ School of Biology, Ecology and Earth Sciences, University of New South Wales

1st Revision Submitted to Journal of Hydrometeorology

October 2016

Abstract

Rainfall variability in the Tigris-Euphrates Headwaters is a result of interaction between topography and meteorological features at a range of spatial scales. Here, we have implemented the Weather Research and Forecasting (WRF) model, driven by NCEP/DOE R2, to better understand these interactions. Simulations were performed over a domain covering most of the Middle-East. The extended simulation period (1983-2013) enables us to study seasonality, interannual variability, spatial variability and extreme events of rainfall. Results showed that the annual cycle of precipitation produced by WRF agrees much more closely with observations than does R2. This was particularly evident during the transition months of April and October, which were further examined to study the underlying physical mechanisms. In both months, WRF improves representation of interannual variability relative to R2, with a substantially larger benefit in April. This improvement results primarily from WRF's ability to resolve two low-level terrain-induced flows in the region that are either absent or weak in NCEP/DOE: one parallel to western edge of the Zagros Mountains, and one along the East Turkish Highlands. The first shows a complete reversal in its direction during wet and dry days: when flowing southeasterly it transports moisture from the Persian Gulf to the region, and when flowing northwesterly it blocks moisture and transports it away from the region. The second is more directly related to synoptic-scale systems and carries moist, warm air from the Mediterranean and Red Seas toward the region. The combined contribution of these flows explains about 50% of interannual variability in both WRF and observations for April and October precipitation.

1. INTRODUCTION

Interannual precipitation variability has profound impacts on environment, water resources, and, potentially, socio-economic development and political stability in water stressed regions. The implications of these impacts can be particularly important in highly utilized transboundary rivers like the Tigris-Euphrates system. The Tigris-Euphrates Headwaters (TEH) are located in a predominantly Kurdish region divided between three different countries: Turkey, Iraq and Syria (Figure 1). A number of tributaries from Iran also contribute to the Tigris River discharge. Iraq and Syria, the two downstream riparian States of the Tigris-Euphrates system, have two of the highest ratios of surface water dependency in the Middle East and North Africa (Tropp and Jagerskog, 2006). This underscores the significance of agreements on water allocation between the four countries that share the basin. In recent years there have been a number of attempts to reach bilateral protocols, but successful basin-wide cooperation does not exist. The increase in water demand and frequency of severe droughts in recent decades (Hoerling et al., 2012) can exacerbate regional conflicts and intensify the long-standing political instability in the region. For example, the initiation of the recent ongoing civil war in Syria, which has greatly affected global security, has been partly attributed to the regional droughts (Gleick, 2014; Kelley et al. 2015). This may be due to the fact that agriculture is the largest surface water consumer in the region, and consequently the economic prosperity of people primarily depends on the amount of precipitation over the TEH (UN-ESCWA and BGR, 2013). In addition, one of the major dust source points in the Middle East is located within and downstream of the TEH (Cao et al., 2015; Moridnejad, 2015). This implies that the soil moisture influenced by precipitation variability in

the region (Zaitchik et al. 2007a) can have significant health impacts on the people of Syria, Iraq and the downwind countries (Soleimani et al. 2015).

Precipitation in the TEH is a result of interaction between topography and several different meteorological features that act at regional and global scales (Evans et al. 2004). During the cold season, in particular, precipitation is largely controlled by westerly storm tracks of mid-latitude synoptic-scale disturbances (Türkes 1998; Trigo et al., 2002; Evans et al. 2004). These storm tracks are influenced by large-scale teleconnection phenomena, including the El Niño-Southern Oscillation (ENSO) and the North Atlantic Oscillation (NAO) (Barlow et al., 2015), which modify track location and can also modulate the moisture flux toward the region through Rossby wave propagation or other mechanisms (e.g., Cullen and Demenocal, 2000; Barlow et al., 2002; Mariotti, 2007; Kahya, E., 2011; Dezfuli et al., 2010; Donat et al., 2014).

At regional scale, two low-level topographically-driven jets have been found to modulate climate variability over the area: the Shamal winds, and the Zagros Barrier Jet (ZBJ). The Shamal winds flow north-northwesterly, parallel to the Zagros Mountains toward the Persian Gulf, and are most notably present during winter and summer. The relative intensity and spatial expansion of three pressure cells contribute to formation and intensity of the Shamals (e.g., Hamidi et al. 2013; Yu et al. 2016): the semi-permanent high pressure over the northwestern Arabian Peninsula, heat-low over Iran and Pakistan, and an anomalous high-pressure area over east Mediterranean. The summer Shamal winds can be further intensified due to the terrain-induced pressure gradient and friction forces along the Zagros Mountains (Zarrin et al. 2011; Giannakopoulou and Toumi, 2012). The subsidence associated with the thermodynamically-driven circulation from the Zagros Plateau can suppress the precipitation in

the upwind region, particularly in the transitional months of April and May (Zaitchik et al. 2007b). The ZBJ, on the other hand, flows southeasterly along the western slopes of the Zagros Mountains, and advects warm, moist air from the Persian Gulf into the TEH (Evans and Smith 2006). This terrain-induced jet, which has a significant impact on precipitation over the region, may be resolved only with high-resolution wind data that can be provided by regional climate models (RCMs). Understanding the ZBJ's behavior is crucial as it provides a dynamical link between water vapor in southern Mesopotamia, which is increasing due to global warming, to precipitation variability in the TEH (Evans 2008; Evans and Alsamawi 2011). This is particularly important during the transition seasons (Evans 2008). Previous RCM studies of regional atmospheric dynamics have focused either on a limited number of years or a single event (Evans et al. 2004; Evans and Smith 2006; Giannakopoulou and Toumi, 2012). Therefore, the regional controls on the interannual variability of rainfall have not been fully understood.

Here, we perform a 31-year regional climate simulation to examine the contribution of low-level terrain-induced winds to the rainfall variability over the TEH. The data, model configuration, and the analysis approach are presented in Sections 2 and 3. The long duration of the simulations enables us to study seasonality, interannual variability, and spatial variability of rainfall over the region (Section 4). The general synoptic-scale patterns of the atmosphere during wet and dry days are briefly discussed in Section 5. This is followed by an analysis of the meso-scale systems with an emphasis on the role of low-level moisture transport on rainfall variability (Section 6). Concluding remarks are offered in Section 7.

2. DATA, MODEL DESCRIPTION AND ANALYSIS APPROACH

109 Atmospheric reanalysis data sets are generally too coarse to adequately capture meso-scale
110 phenomena. In addition, diagnostic variables such as precipitation are a direct output of the
111 global climate model (GCM) that is used for the reanalysis; the GCM used in NCEP/DOE AMIP-II
112 Reanalysis for instance, is nudged toward the atmosphere through data assimilation (Kistler et
113 al., 2001), but precipitation observations are not assimilated by any of the most widely used
114 global reanalysis systems. Thus, reanalysis precipitation estimates should be used with extreme
115 caution. However, many gridded precipitation data sets, which are based on ground or satellite
116 observations, or the combination of both, are available, though each has its own limitations.
117 Depending on the application, the limiting factors may include one or more of the following:
118 low temporal resolution (e.g., available monthly only); coarse spatial resolution; available over
119 a period that is too short for interannual variability analysis; misrepresentation of precipitation
120 over regions with complex topography or strong convection. A full intercomparison of different
121 precipitation products is not a focus of the current study. However, in order to detect any
122 potential inconsistency, we have performed pair-comparison between a select number of these
123 data sets by examining the annual cycle, interannual variability, frequency distribution of daily
124 data, and long-term mean differences, where applicable. The results (not shown) led us to
125 choose the data provided by the Global Precipitation Climatology Centre (GPCC) for evaluating
126 the model outputs. The GPCC offers monthly and daily products, which respectively cover the
127 entire and most of the study period, and it uses rain-gauge data with a good coverage over the
128 TEH. The monthly product, GPCC Full Data Reanalysis Version 7.0, is available over the period
129 1901-2013 at 0.5° and 1° grid resolutions (Schneider et al., 2015). The daily product, GPCC Full

Data Daily Version 1.0, is available for the period 1988-2013 at 1° grid resolution (Schamm et al., 2015). For consistency, we have used 1°-grid data for both monthly and daily analysis.

The shortcomings in atmospheric reanalysis products and precipitation data sets, mentioned above, have made it difficult to study meso-scale phenomena. A common practice to tackle this issue is to perform dynamical downscaling using RCMs that are driven by reanalysis data. Here, we use the Advanced Research Weather Research and Forecasting (WRF) model version 3.6 over a domain spanning most parts of the Middle East (32-56E; 25-45N, Fig. 1). The WRF model is a numerical weather prediction and atmospheric simulation system that incorporates the fully compressible, non-hydrostatic Euler equations (Skamarock et al., 2008). It includes a large number of physics schemes, used for parameterization of the processes that cannot be resolved by the model. The initial and boundary conditions used for the model runs are from the NCEP/DOE AMIP-II Reanalysis (Reanalysis-2) Daily Averages at $2.5^\circ \times 2.5^\circ$ resolution, hereafter referred to as “NCEP.”

The model simulations provide a complete high-resolution set of many different land and atmospheric variables. Composites of dry and wet days will be formed, and a suite of moisture flux variables from the model outputs will be analyzed and compared to the reanalysis data. That allows us to better understand the meso-scale mechanisms, contributing to the interannual variability of rainfall and extreme daily events, as well as the capability of the NCEP data in resolving such processes.

3. MODEL CONFIGURATION

We perform 31 years of WRF model simulations (1983-2013) over the study domain shown in Fig. 1. The analysis, however, focuses on the TEH region, which is located just to the northwest of the domain center (40-44E; 36-40N). The model was implemented at 27km resolution with 40 vertical levels. The physics parameterization options were chosen based on the sensitivity analysis on a select number of years (not shown), using several different physics combinations suggested in previous studies (e.g., Argüeso et al., 2011; Giannakopoulou and Toumi, 2012; Efsthathiou et al., 2013; Zittis et al., 2014). The set of physics schemes that we have used include the Community Atmosphere Model (CAM) Version 5.1 (Neale et al., 2010) for microphysics, CAM Version 3 (Collins et al., 2004) for both longwave and shortwave radiation, the Noah land surface model (Ek et al., 2003) for land surface processes, the Yonsei University scheme (Hong et al. 2006) for planetary boundary layer processes, and the Kain-Fritsch cumulus scheme (Kain and Fritsch, 1990). However, our sensitivity analysis showed that, replacing the three CAM options, respectively with the WRF Single Moment Microphysics 3 class scheme (WSM3) (Hong et al. 2004), the Rapid Radiative Transfer Model (RRTM) (Mlawer et al. 1997) for longwave radiation, and the Dudhia (1989) scheme for shortwave radiation, would yield very similar results.

A known undesirable consequence of long-term simulations by RCMs is the slow departure of the large-scale climate state from the data used to drive the model (Pohl et al., 2011). To address this issue, we reinitialized the simulations each year, resulting in 31 separate model runs. Each run is 15 months long, starting from June 1 and ending on September 1 of the following year. The first three months are used to spin-up the model and are discarded. This is done to approach a dynamical equilibrium for the slowly-varying surface variables such as soil

moisture, which presents minimal interannual memory in the region. A sensitivity analysis for a select number of years was performed to evaluate the effects of the start date of reinitialization and the length of spin-up, varying from June to November. The WRF outputs did not present any noticeable changes to different values of these measures (not shown).

4. EVALUATION OF MODEL PRECIPITATION

Simulated 31-year monthly precipitation totals over TEH are evaluated against GPCC data. The precipitation provided by the NCEP is also compared with the GPCC product and WRF results to examine the potential advantages of the dynamical downscaling for regional climate studies when compared to coarse reanalysis data.

4.1. ANNUAL CYCLE

Results showed that the annual cycle of precipitation produced by WRF agrees much more closely with the observations than does the original NCEP product (Fig 2a). During the dry season (June-August), both NCEP and WRF overestimate the precipitation total, although the NCEP bias is about 2.5 times larger than the WRF bias. Bias is defined as the ratio of long-term mean seasonal precipitation total of the model (WRF or NCEP) to the GPCC. During the rainy season of November-March, the bias for WRF and NCEP precipitation is about .9 and .5, respectively. The bias of the downscaled precipitation results is particularly small in the transition months of April and October. The rest of this paper is devoted to further examining the precipitation mechanisms of these two months, which have been less studied than the main rainy season, despite their combined 21% contribution to the annual total. A sharp change

in convective component of the total rainfall is evident during these two months (Fig. 2b). April, with a mean total rainfall of 73 mm in the TEH, is the start of the growing season (Barlow et al., 2015), and reflects the transition from primarily non-convective winter rainfall to convectively-driven summer rainfall. In contrast, October, which has a mean total rainfall of 41 mm, shows the transition from convective to non-convective rainfall. Although the shape of the annual cycle of the convective-to-total rainfall is very similar for both WRF and NCEP, the magnitude of this ratio is about 75% for WRF and 90% for NCEP. The different magnitudes of total rainfall and contribution of the convection in WRF and NCEP may underscore the importance of resolving regional features, including topography, in precipitation variability in these months.

4.2. INTERANNUAL VARIABILITY

The TEH is the rainy part of the Tigris-Euphrates Basin in April and October, and downstream regions receive little or no rain (Fig 3a,d). In spite of the relatively large difference in mean daily precipitation rate between these two months, this latitudinal contrast is apparent in both months with a generally similar pattern. However, the border between dry and wet regions in October extends farther north and reaches the southern edge of the TEH.

In order to evaluate WRF performance in simulating interannual precipitation variability, the time series of WRF and NCEP precipitation in April and October over the period 1983-2013 are compared with the GPCC data set (Fig. 3, middle). In both months, the precipitation provided by WRF shows higher correlations with observations, with a substantially larger benefit in April. The correlation coefficients between GPCC data and precipitation simulated by WRF and NCEP models are, respectively .84 and .30 for April, and .85 and .69 for October. In

spite of some year-to-year variability, the NCEP model, overall, underestimates the precipitation in both months. Analysis of the histograms of daily precipitation of all three data sets over the entire 31-year study period suggest that one reason for WRF's improvement over NCEP is its ability to simulate daily extremes (Fig. 3c,f). The comparison shows that the 90th percentile value of the WRF results is very close to the GPCC, whereas the NCEP has a lower value in both transition months.

4.3. SPATIAL VARIABILITY

Maps of climate regions are most typically generated on the basis of long-term mean climate conditions (e.g., Koppen, 1936). Spatial patterns of long-term mean conditions, however are not necessarily aligned with those of common interannual variability, because the driving factors of the two can be quite different (Dezfuli and Nicholson, 2013). Here we are concerned with spatial patterns of interannual precipitation variability in our study months, which requires an objective evaluation to identify regions of homogeneity. We do this using regionalization criteria suggested by Dezfuli (2011), implemented with the *HiClimR* R package (Badr et al., 2014) described by Badr et al. (2015). This open-source package is designed specifically for climate regionalization, and has been applied in several case studies (e.g., Berhane et al., 2015; Badr et al., 2016).

Prior to regionalization the 31-year, gridded precipitation records were standardized and their linear trend was removed. These ensures that spatial patterns represent interannual variability, and all grids with various precipitation magnitudes and trends are equally incorporated into the regionalization process. Grid cells with close-to-zero mean or standard

deviation were masked to avoid artifacts that can be introduced by low signal, nearly precipitation free areas. In addition, the detrended, standardized data were replaced with the leading principle components that collectively account for at least 70% of the variance. This helps to isolate the random noise in data and to produce contiguous regions (Dezfuli, 2011). The clustering algorithm employed is the “regional linkage” method, proposed by Badr et al (2015) as an alternative to the existing hierarchical clustering techniques. The regional linkage method minimizes the inter-regional correlation between region means at each merging step of the hierarchical process. This technique allows us to identify and remove the spatial noise in data that are manifested as very small regions with a small number of grid points.

The regionalization results based on the interannual variability of rainfall during the period 1983-2013, using GPCC, WRF and NCEP data are shown in Fig. 4. We have optimized the regionalization parameters for the GPCC data, based on the guidelines suggested in previous studies, discussed above. That resulted in dividing the study domain into two homogeneous sub-regions for both months. The TEH is located within the limits of one of these sub-regions, although in October a small part of the northwestern corner of the TEH is placed in a different sub-region. The spatial patterns resulting from GPCC and WRF are very similar, which underscores the capability of WRF model to capture the character of interannual variability over the entire domain. However, the regionalization based on NCEP shows large disagreements with GPCC, particularly in April. During this month, the GPCC and WRF dominant spatial variability is in the zonal direction, whereas the NCEP regions are identified in the meridional direction. In October, all three datasets yield two sub-regions that are separated

along the SW-NE direction. NCEP, however, places the border between regions directly across our TEH focus area, where WRF and GPCC place it in the upper NW corner of the focus area.

5. SYNOPTIC-SCALE PATTERNS: WET VS. DRY DAYS

Statistical analysis presented in Section 4 shows that the spatio-temporal variability and extreme daily events of the GPCC and WRF rainfall are in good agreement. This consistency allows us to leverage the high-resolution WRF outputs that offer five additional years (1983-1987), when compared to GPCC daily data. The long-period daily precipitation provided by the WRF model, enables us to better understand the properties of the regional climate, including the dominant processes during wet and dry days. We have compiled a wet composite, which includes days that the WRF rainfall, averaged over TEH, is greater than its 90th percentile over the period 1983-2013. Similarly, the dry composite includes days that the regional mean rainfall is less than its 10th percentile. We have analyzed some aspects of the synoptic-scale systems during these two composites. The WRF domain is not large enough to provide a full picture of these systems. For this reason, we use the NCEP data, which are sufficient to resolve large-scale atmospheric phenomena.

A full diagnostic analysis, using the NCEP data, is beyond the scope of this work. However, we have analyzed selected atmospheric variables that can give us some insight into the synoptic-scale processes in the region. The composites of geopotential height and horizontal wind vectors at 700 hPa are analyzed for April and October (Fig. 5). Choosing the 700 hPa level enables us to remain reasonably above the surface and therefore avoid artifacts in the reanalysis data due to the varying terrain in the region, while capturing characteristics

representative of the lower troposphere. During the wet composite in April, the TEH lies at the leading edge of strong troughs, which are associated with cyclonic vorticity advection and warm, moist air transport from the Mediterranean and the Northern Red Sea toward the region. These can provide favorable conditions for rainfall events. During the dry days, these features are not present: weak troughs move northwestward, far from the TEH, and the moisture flux toward the region is weak. However, the semi-permanent high-pressure cell, located over the southern parts of the Arabian Peninsula, does not show a significant contrast between the wet and dry composites. The synoptic-scale patterns in October are generally similar to those in April, particularly during the wet composite. The high-pressure cell, however, shifts northward, when compared to April, and is slightly stronger and located more over the center of the Arabian Peninsula during the dry composite. In addition, the mid-latitude trough does not exist in the dry days.

6. MESO-SCALE SYSTEMS

Synoptic-scale phenomena can be captured by reanalysis data, and dynamical downscaling may offer only minor advantages. In fact, in some cases dynamical downscaling can degrade representation of large-scale features relative to reanalysis (e.g. Castro et al. 2005). However, some of the meso-scale phenomena are actually driven by the synoptic-scale systems, and thus the NCEP-based analysis, discussed above, becomes relevant and can be used as a guideline for detecting these features.

6.1. ZAGROS BARRIER JET AND SHAMAL WINDS

During the wet composite (Figs. 5a, c), the northwest-southeast orientation of the pressure gradient, which is parallel to the Zagros mountains, and the low-level winds perpendicular to that line can set up favorable conditions for the southeasterly barrier jet, ZBJ. The jet can be detected by examining the near-surface horizontal wind vectors drawn from WRF simulations (Figs 6a, c). The ZBJ follows the terrain and its mean speed during the wet composite is greatest at about 34-35N with a magnitude of about 7 and 6 m/s for April and October, respectively (Table 1). The corresponding wind speeds in the NCEP data (Figs 6b, d) are, respectively about 2 and 1 m/s for these two months. These differences are statistically significant at 1% level, using a two-tailed Student t-test. In addition, due to the coarse resolution of the NCEP data, NCEP winds do not follow the terrain when there is a sharp topographical contrast. The improvement in resolving meso-scale features resulting from downscaling is clearly manifested in the patterns of low-level (925-850 hPa) geopotential heights (Fig 6). Although, as expected, the general spatial patterns for the NCEP data and WRF are similar, the details provided by the latter enables us to identify the barrier jet. The geopotential height contours are set up such that the flow is correctly directed along the terrain edge, and the pressure gradient controlling the jet intensity is stronger in WRF results. The jet is strongest below the crest level, as expected for classic barrier jets (Kingsmill et al., 2013; Neiman et al. 2013).

During dry days (Fig. 7), the wind direction between the TEH and the Persian Gulf is northwesterly, opposite to that in the wet composite. These northwesterly winds are more horizontally expanded than the ZBJ, and resemble the characteristics of the Shamal winds, which are partly controlled by the heat low over the Iranian Plateau (Zaitchik et al., 2007b; Hamidi et al. 2013; Yu et al. 2016). This is consistent with the patterns of the WRF geopotential

heights, which are not well-resolved in the NCEP data. This could be the reason that the NCEP winds blow northeasterly, rotated approximately 90 degrees from the WRF wind direction.

To further investigate the variability of daily wind in the TEH-Persian Gulf corridor, the time series of the regional mean (34.5-35.5N, 43.5-45E) meridional wind is used as an index of wind intensity, particularly the ZBJ (Fig 8). Although the long-term mean of the daily meridional wind is slightly greater than zero, the wind shows a strong day-to-day variability, with maximum values reaching 20 and 16 m/s during April and October (Table 1). Although the frequency of the positive and negative wind events is fairly comparable in both months, the histograms of the daily meridional wind are skewed toward the positive values (Figs. 8b,d). This is evident in the greater absolute magnitude of the 90th percentiles than the 10th percentiles, which can be considered as thresholds for extreme events.

The reversal of the wind direction between wet and dry composites implies that the ZBJ and Shamal can modulate the moisture supply over the TEH. The moisture flux by near-surface winds confirms this, as shown in Fig. 9. The moisture flux vectors depict the advection of the warm, moist air by the ZBJ toward the TEH during the wet days. The magnitude of these vectors, which are quite similar in both transition months, suggests that the air, as it moves along the terrain, sustains a high amount of moisture throughout its path to the TEH. In contrast, the northwesterly Shamal-like winds block the moisture and transport it away from the region, resulting in dry conditions (Figs. 9b,e). The histograms of the daily meridional moisture flux, vq , over the representative region (Figs. 9c,f), have an overall similar shape to the histograms of the meridional wind.

Building on this analysis of ZBJ vertical structure and related meridional moisture flux, we produce a composite of high moisture flux by the barrier jet (HMF-ZBJ) by compiling days with vq values higher than their 90th percentile over the representative ZBJ region (yellow strip in Figs. 9a,d). Figure 10 shows a vertical cross-section of vq for this HMF-ZBJ composite in WRF and NCEP data for April and October. In both months, the moisture flux simulated by the WRF model is most intense along the abrupt topographical change, and it reaches its maximum below the 850 hPa level. Its maximum magnitude during April is greater than $6 \times 10^{-2} \text{ ms}^{-1} \text{ g kg}^{-1}$, which is more than two-fold larger than the NCEP moisture flux over the same area. This difference is statistically significant at 1% level. The maximum value of the moisture flux in October is slightly lower than in April, but the difference between NCEP and WRF maintains a similar level of statistical significance. The contrast in moisture flux between the two models in the middle and upper troposphere, which contains less humidity than the lower levels, is small.

The spatial patterns of mean daily precipitation of WRF and NCEP for the HMF-ZBJ composite are compared to assess how the difference in moisture flux between the two models relates to rainfall estimates for the TEH (Fig. 11). Both WRF and NCEP show higher rainfall during positive HMF-ZBJ events. However, the spatial structure of the WRF rainfall composite resembles the long-term mean rainfall pattern, implying that the increase has been quite evenly distributed within the TEH. Such homogeneity, particularly in April, is not evident in the NCEP patterns, which may be associated with its inability to detect spatial variability of rainfall within the region, as shown in Fig. 4. The WRF rainfall amounts are greater than NCEP for the entire region, except during October over a small sector in the southwestern TEH, which has less total rainfall and is also distal to the ZBJ point of entry to the region. The TEH-wide

precipitation difference is statistically significant at 1% level (Figs. 11c,f). The ZBJ-rainfall association depends on the intensity of the jet. Spatial patterns of rainfall for weak and moderate ZBJ events are shown in Fig. 12, and can be compared with strong jets presented in Fig. 11a,d. These are produced based on weak moisture flux (WMF-ZBJ) and moderate moisture flux (MMF-ZBJ) composites, which respectively represent vq ranges of 0.2–0.5 and $1\text{--}2 \times 10^{-2} \text{ ms}^{-1} \text{ g kg}^{-1}$. Comparison of these three conditions clearly shows that the stronger ZBJs bring more precipitation to the region. This association seems to behave differently in April and October. In April, the rainfall over the region increases incrementally as the ZBJ strengthens, while maintaining the general characteristics of the spatial patterns. However, in October, such gradual variation is less obvious, and the rainfall appears to be more strongly determined by the extreme ZBJs.

6.2. LOW-LEVEL WESTERLY (LLW) FLOW

To reveal other possible factors that can explain the differences in rainfall fields of the two models, we have analyzed the rainy days in WRF that are missed by NCEP. To do that, we have compiled a composite, consisting of the days that WRF precipitation averaged over the TEH is greater than its 80th percentile while the NCEP precipitation is less than its median. For this composite, we have examined the moisture influx to the region from the Mediterranean and the Red Seas. Similar to the ZBJ analysis, the vertical cross-section of the zonal moisture flux, uq , along the blue strip (see Fig. 9) has been compared between the WRF and NCEP products (Fig. 13). The results show that the dynamical downscaling enables us to better resolve another terrain-induced low-level moist inflow. This secondary component is more directly related to

the synoptic-scale westerly systems, contributing to the TEH rainfall, and it flows along the East Turkey Highlands. Similar to the ZBJ patterns, the WRF places the maximum moisture inflow along the mountain range, thus within the southern latitudes of the region. However, the moisture fluxes provided by the NCEP data are either weak or pushed southward, away from the TEH. For both months, the differences between the WRF and NCEP are significant at 1% level, using a Student's t-test, although in April, the region of maximum uq is confined within the levels closer to the surface.

Unlike the ZBJ, the LLW does not have the characteristics of classic barrier jets. The westerly flow is not perfectly perpendicular to the mountains, and the direction of the pressure gradient produced by the synoptic systems does not resemble the necessary conditions for a westerly barrier jet. The LLW instead, is a part of the synoptic-scale pressure cells that is modified by the east-west oriented mountains. This low-level flow, therefore, remains nearly geostrophic.

6.3. INTERANNUAL VARIABILITY: RAINFALL vs LOW-LEVEL FLOWS

The strong contribution of the ZBJ and LLW to extreme rainfall events encouraged us to examine their relationship to interannual precipitation variability. For each month an index is defined to represent the combined contributions of the moisture flux by these two low-level flows to total precipitation. These indices, the April Moisture Index (AMI) and the October Moisture Index (OMI), are defined as the summation of standardized extreme vq values over the ZBJ region added to the standardized extreme uq values over the region representing the low-level westerly flow (39-41E, 36-40N). Values of vq and uq that exceed their 80th percentiles

are taken as extreme values. Each month of each year is consequently represented with one value. We then quantify the percentage of interannual precipitation variability in WRF, NCEP, and GPCC that is associated with AMI and OMI. The coefficients of determination (R^2) between rainfall data and their components with these two indices for the 31-year study period are shown in Table 2. The AMI explains 46% of the interannual variability of WRF rainfall, while only 6% of the NCEP rainfall variability is attributed to this index. Although the OMI explains a larger fraction of the variance (30%) of the NCEP rainfall in October than the AMI in April, the contribution of this index to temporal variability of the WRF rainfall (53%) remains significantly larger than NCEP. The fact that each month is represented with one value enables us to find the correlations between the moisture indices and GPCC rainfall for the entire time period. The R^2 values of GPCC for both April (48%) and October (55%) are comparable to the R^2 of WRF, and are in fact slightly larger. These results, including the contrasts between different months and data sets, are consistent with the interannual correlations presented in Section 4.2.

Furthermore, we have calculated the coefficients of determination between the two indices with the convective and non-convective components of WRF and NCEP rainfall. The results show that WRF improvements over NCEP are proportional to its ability to simulate convective rainfall, which is the dominant component in these two months. That can be one explanation for the poor performance of the NCEP during April and its better performance in October.

The partial contribution of the ZBJ and LLW to the monthly rainfall totals in April and October along with the summary of the interannual root mean square errors (RMSE) and correlation coefficients between each model and GPCC are presented in Table 3. For both months, the mean rainfall total associated with the composite of extreme ZBJ events has a

larger contribution to the total monthly means than the composite of the LLW flow. These ratios for NCEP are just slightly lower than in WRF. However, NCEP underestimates the rainfall amount and poorly detects interannual variability, as manifested in high RMSE and low correlation coefficient values relative to WRF. Note that ZBJ and LLW events frequently occur independently of each other—ZBJ + LLW events only represent about 30% of total ZBJ events and total LLW events. This implies that, to a large degree, the two low-level flows act independently. Moreover, we calculated the coefficient of determination between WRF rainfall and monthly mean vq values over the ZBJ region that are greater than their 80th percentile. The R^2 values for April and October are 0.32 and 0.5, respectively. This further indicates that the AMI and OMI are largely determined by the ZBJ, particularly in October, and the LLW contributes as a secondary component in interannual variability.

7. DISCUSSION AND CONCLUSIONS

Previous regional climate modeling studies on precipitation processes over the Tigris-Euphrates Headwaters have been limited to a small number of years or events. The 31-year WRF simulation in the current study, driven by the NCEP data, has enabled us to analyze seasonality, interannual variability, spatial variability and extreme events of rainfall over the region. For instance, several studies conducted by Evans and colleagues over a 5-year period have examined the 200 largest precipitation events, of which only about 30 cases occurred during April and October, the two transition months investigated in this paper (Evans et al. 2004; Evans and Smith 2006; Evans 2008). We have incorporated about 650 extreme events to

compile the AMI and OMI indices, which are used to explain the interannual variability of rainfall in these two transitional months.

In addition, other studies have tried to explain the interannual variability mainly by teleconnections. However, our high resolution long period simulation has allowed us to show that the regional features, which can be detected by mesoscale models, explain about half the interannual variability. These features, which are unresolved or weak in the NCEP data, include the Zagros Barrier Jet (ZBJ), the Shamal winds, and the low-level westerly flow; the latter is a part of the synoptic systems affecting the rainfall of the region.

The ZBJ and Shamals flow parallel to the western edge of the Zagros Mountains in southeasterly and northwesterly direction, respectively, and therefore transport moisture toward and away from the Tigris-Euphrates Headwaters. This results in wet conditions during ZBJ active days and dry conditions during strong Shamals. However, association between rainfall of the TEH and these two terrain-induced wind flows is nonlinear as the ZBJ and Shamals are not controlled by opposite atmospheric conditions.

The ZBJ is a barrier jet, and it occurs when its favorable conditions exist: stably stratified winds perpendicular to the mountains and pressure gradient along the terrain line. The contribution of this jet to monthly rainfall is proportional to its intensity. However, while this association is quite linear for April, it appears that the extreme ZBJs in October make a disproportionally higher contribution to rainfall totals than do the weak and moderate jets.

The Shamals, on the other hand, are not barrier jets; these are formed and controlled by three synoptic-scale pressure cells in the region: two high pressure areas over the Arabian Peninsula and eastern Mediterranean, and a heat-low over Iran. It seems that the heat low over

the Iranian Plateau has the strongest contribution to the Shamal winds presented in this study. We speculate that this may be a characteristic of early season Shamals. The summer Shamals, for instance, are most active during June and July, but their onset can be as early as mid-April (Yu et al. 2016). Further studies are required to investigate the drivers and characteristics of the Shamals during transition seasons and their differences with those of the boreal summer.

Another topographic-driven flow that affects the rainfall variability of the region is the LLW flow, which is embedded in the westerly synoptic systems. This flow, which is not well-resolved in NCEP, transports moisture from the Mediterranean and Red Seas toward the region, and is modified by the southern edge of the East Turkish Highlands. The contribution of LLW is secondary to the role of low-level winds along the Zagros Mountains, particularly in October. However, the combined contribution of these two explains about 50 percent of the interannual variability of April and October rainfall in observations and in our WRF simulations. These results are intriguing because the ZBJ, Shamals and LLW flow are most likely not well-resolved in future projections provided by the coarse-resolution GCMs used in the Coupled Model Intercomparison Project Phase 5 (CMIP5). A similar approach to the current study can be applied to the outputs of those GCMs, and that will enable us to better understand the potential non-stationary change in future interannual variability of rainfall. Such changes are expected as global warming alters storm tracks, atmospheric stability patterns, and specific humidity, which all affect the dynamics of these flows and/or the magnitude of their impact on precipitation.

499 **ACKNOWLEDGMENTS**

500 We would like to thank Darryn Waugh of JHU, Ronald Smith of Yale, two anonymous reviewers
501 and the Editor, Ruby Leung for constructive comments. This work was supported by the Food
502 and Agriculture Organization and by NASA Applied Sciences Program award 13-WATER13-0010.
503 Computational resources were provided by the Homewood High Performance Cluster of the
504 Johns Hopkins University and by NSF-MRI Grant CNS-0821794, MRI-Consortium: Acquisition of
505 a Supercomputer by the Front Range Computing Consortium (FRCC), with additional support
506 from the University of Colorado and NSF sponsorship of the National Center for Atmospheric
507 Research.

508

References:

- Argüeso, D., Hidalgo-Muñoz, J.M., Gámiz-Fortis, S.R., Esteban-Parra, M.J., Dudhia, J. and Castro-Díez, Y., 2011. Evaluation of WRF parameterizations for climate studies over Southern Spain using a multistep regionalization. *Journal of Climate*, 24(21), pp.5633-5651.
- Badr, H.S., Zaitchik, B.F. and Dezfuli, A.K., 2014. HiClimR: Hierarchical climate regionalization. *Comprehensive R Archive Network (CRAN)*. [Available online at <http://cran.r-project.org/package=HiClimR>.]
- Badr, H.S., Zaitchik, B.F. and Dezfuli, A.K., 2015. A tool for hierarchical climate regionalization. *Earth Science Informatics*, 8(4), pp.949-958.
- Badr, H.S., Dezfuli, A.K., Zaitchik, B.F. and Peters-Lidard, C.D., 2016. Regionalizing Africa: Patterns of Precipitation Variability in Observations and Global Climate Models. *J. Climate (in press)*.
- Barlow, M., Cullen, H. and Lyon, B., 2002. Drought in central and southwest Asia: La Niña, the warm pool, and Indian Ocean precipitation. *Journal of Climate*, 15(7), pp.697-700.
- Barlow, M., Zaitchik, B., Paz, S., Black, E., Evans, J. and Hoell, A., 2015. A Review of Drought in the Middle East and Southwest Asia. *Journal of Climate*, (2015).

531 Berhane, F., Zaitchik, B. and Badr, H.S., 2015. The Madden–Julian Oscillation’s Influence on
532 Spring Rainy Season Precipitation over Equatorial West Africa. *Journal of Climate*, 28(22),
533 pp.8653-8672.

534

535 Cao, H., Amiraslani, F., Liu, J. and Zhou, N., 2015. Identification of dust storm source areas in
536 West Asia using multiple environmental datasets. *Science of the Total Environment*, 502,
537 pp.224-235.

538

539 Castro, C.L., Pielke, R.A. and Leoncini, G., 2005. Dynamical downscaling: Assessment of value
540 retained and added using the Regional Atmospheric Modeling System (RAMS). *Journal of*
541 *Geophysical Research: Atmospheres*, 110(D5).

542

543 Collins, W.D., Rasch, P.J., Boville, B.A., Hack, J.J., McCaa, J.R., Williamson, D.L., Kiehl, J.T.,
544 Briegleb, B., Bitz, C., Lin, S.J. and Zhang, M., 2004. Description of the NCAR community
545 atmosphere model (CAM 3.0). *NCAR Tech. Note NCAR/TN-464+ STR*, 226.

546

547 Cullen, H.M. and Demenocal, P.B., 2000. North Atlantic influence on Tigris–Euphrates
548 streamflow. *International journal of climatology*, 20(8), pp.853-863.

549

550 Dezfuli, A.K., Karamouz, M. and Araghinejad, S., 2010. On the relationship of regional
551 meteorological drought with SOI and NAO over southwest Iran. *Theoretical and applied*
552 *climatology*, 100(1-2), pp.57-66.

553

554 Dezfuli, A.K., 2011. Spatio-temporal variability of seasonal rainfall in western equatorial Africa.

555 *Theoretical and applied climatology*, 104(1-2), pp.57-69.

556

557 Dezfuli, A.K. and Nicholson, S.E., 2013. The relationship of rainfall variability in western

558 equatorial Africa to the tropical oceans and atmospheric circulation. Part II: The boreal autumn.

559 *Journal of Climate*, 26(1), pp.66-84.

560

561 Donat, M.G., Peterson, T.C., Brunet, M., King, A.D., Almazroui, M., Kolli, R.K., Boucherf, D., Al-

562 Mulla, A.Y., Nour, A.Y., Aly, A.A. and Nada, T.A.A., 2014. Changes in extreme temperature and

563 precipitation in the Arab region: long-term trends and variability related to ENSO and NAO.

564 *International Journal of Climatology*, 34(3), pp.581-592.

565

566 Dudhia, J., 1989. Numerical study of convection observed during the winter monsoon

567 experiment using a mesoscale two-dimensional model. *Journal of the Atmospheric Sciences*,

568 46(20), pp.3077-3107.

569

570 Efstathiou, G.A., Zoumakis, N.M., Melas, D., Lolis, C.J. and Kassomenos, P., 2013. Sensitivity of

571 WRF to boundary layer parameterizations in simulating a heavy rainfall event using different

572 microphysical schemes. Effect on large-scale processes. *Atmospheric Research*, 132, pp.125-

573 143.

574

575 Ek, M.B., Mitchell, K.E., Lin, Y., Rogers, E., Grunmann, P., Koren, V., Gayno, G. and Tarpley, J.D.,
576 2003. Implementation of Noah land surface model advances in the National Centers for
577 Environmental Prediction operational mesoscale Eta model. *Journal of Geophysical Research:*
578 *Atmospheres*, 108(D22).

579

580 Evans, J.P., Smith, R.B. and Oglesby, R.J., 2004. Middle East climate simulation and dominant
581 precipitation processes. *International Journal of Climatology*, 24(13), pp.1671-1694.

582

583 Evans, J.P. and Smith, R.B., 2006. Water vapor transport and the production of precipitation in
584 the eastern Fertile Crescent. *Journal of Hydrometeorology*, 7(6), pp.1295-1307.

585

586 Evans, J.P., 2008. Changes in water vapor transport and the production of precipitation in the
587 eastern fertile crescent as a result of global warming. *Journal of Hydrometeorology*, 9(6),
588 pp.1390-1401.

589

590 Evans, J.P. and Alsamawi, A., 2011. The importance of the Zagros Mountains barrier jet to
591 future precipitation in the Fertile Crescent. *Open Atmospheric Science Journal*, 5, pp.87-95.

592

593 Giannakopoulou, E.M. and Toumi, R., 2012. The Persian Gulf summertime low-level jet over
594 sloping terrain. *Quarterly Journal of the Royal Meteorological Society*, 138(662), pp.145-157.

595

596 Gleick, P.H., 2014. Water, drought, climate change, and conflict in Syria. *Weather, Climate, and*
597 *Society*, 6(3), pp.331-340.

598

599 Hamidi, M., Kavianpour, M.R. and Shao, Y., 2013. Synoptic analysis of dust storms in the Middle
600 East. *Asia-Pacific Journal of Atmospheric Sciences*, 49(3), pp.279-286.

601

602 Hoerling, M., J. Eischeid, J. Perlwitz, X. Quan, T. Zhang, and P. Pegion, 2012: On the increased
603 frequency of Mediterranean drought. *J. Climate*, **25**, 2146–2161, doi:10.1175/JCLI-D-11-
604 00296.1.

605

606 Hong, S.Y., Dudhia, J. and Chen, S.H., 2004. A revised approach to ice microphysical processes
607 for the bulk parameterization of clouds and precipitation. *Monthly Weather Review*, 132(1),
608 pp.103-120.

609

610 Hong, S.Y., Noh, Y. and Dudhia, J., 2006. A new vertical diffusion package with an explicit
611 treatment of entrainment processes. *Monthly Weather Review*, 134(9), pp.2318-2341.

612

613 Kahya, E., 2011. The Impacts of NAO on the Hydrology of the Eastern Mediterranean. In
614 *Hydrological, Socioeconomic and Ecological Impacts of the North Atlantic Oscillation in the*
615 *Mediterranean Region* (pp. 57-71). Springer Netherlands.

616

617 Kain, J.S. and Fritsch, J.M., 1990. A one-dimensional entraining/detraining plume model and its
618 application in convective parameterization. *Journal of the Atmospheric Sciences*, 47(23),
619 pp.2784-2802.

620 Kelley, C.P., Mohtadi, S., Cane, M.A., Seager, R. and Kushnir, Y., 2015. Climate change in the
621 Fertile Crescent and implications of the recent Syrian drought. *Proceedings of the National*
622 *Academy of Sciences*, 112(11), pp.3241-3246.

623

624 Kingsmill, D.E., Neiman, P.J., Moore, B.J., Hughes, M., Yuter, S.E. and Ralph, F.M., 2013.
625 Kinematic and thermodynamic structures of Sierra barrier jets and overrunning atmospheric
626 rivers during a landfalling winter storm in northern California. *Monthly Weather Review*, 141(6),
627 pp.2015-2036.

628

629 Kistler, R., Collins, W., Saha, S., White, G., Woollen, J., Kalnay, E., Chelliah, M., Ebisuzaki, W.,
630 Kanamitsu, M., Kousky, V. and van den Dool, H., 2001. The NCEP-NCAR 50-year reanalysis:
631 Monthly means CD-ROM and documentation. *Bulletin of the American Meteorological society*,
632 82(2), pp.247-267.

633

634 Köppen, W., 1936. Das geographische System der Klimate In: W. Köppen and G. Geiger, ed.
635 *Handbuch der Klimatologie (Handbuch der Klimatologie, vol. 1: C. Gebr, Borntraeger)*.

636

637 Mariotti, A., 2007. How ENSO impacts precipitation in southwest central Asia. *Geophysical*
638 *Research Letters*, 34(16).

639

640 Mlawer, E.J., Taubman, S.J., Brown, P.D., Iacono, M.J. and Clough, S.A., 1997. Radiative transfer
641 for inhomogeneous atmospheres: RRTM, a validated correlated-k model for the longwave.
642 *Journal of Geophysical Research: Atmospheres*, 102(D14), pp.16663-16682.

643

644 Moridnejad, A., Karimi, N. and Ariya, P.A., 2015. A new inventory for middle east dust source
645 points. *Environmental monitoring and assessment*, 187(9), pp.1-11.

646

647 Neale, R.B., Chen, C.C., Gettelman, A., Lauritzen, P.H., Park, S., Williamson, D.L., Conley, A.J.,
648 Garcia, R., Kinnison, D., Lamarque, J.F. and Marsh, D., 2010. Description of the NCAR
649 community atmosphere model (CAM 5.0). *NCAR Tech. Note NCAR/TN-486+ STR*.

650

651 Neiman, P.J., Hughes, M., Moore, B.J., Ralph, F.M. and Sukovich, E.M., 2013. Sierra barrier jets,
652 atmospheric rivers, and precipitation characteristics in Northern California: A composite
653 perspective based on a network of wind profilers. *Monthly Weather Review*, 141(12), pp.4211-
654 4233.

655

656 Pohl, B., Crétat, J. and Camberlin, P., 2011. Testing WRF capability in simulating the atmospheric
657 water cycle over Equatorial East Africa. *Climate Dynamics*, 37(7-8), pp.1357-1379.

658

659 Schamm, Kirstin; Ziese, Markus; Raykova, Kristin; Becker, Andreas; Finger, Peter; Meyer-
660 Christoffer, Anja; Schneider, Udo (2015): GPCC Full Data Daily Version 1.0 at 1.0°: Daily Land-

661 Surface Precipitation from Rain-Gauges built on GTS-based and Historic Data. DOI:
 662 [10.5676/DWD_GPCC/FD_D_V1_100](https://doi.org/10.5676/DWD_GPCC/FD_D_V1_100)
 663
 664 Schneider, Udo; Becker, Andreas; Finger, Peter; Meyer-Christoffer, Anja; Rudolf, Bruno; Ziese,
 665 Markus (2015): GPCC Full Data Reanalysis Version 7.0 at 0.5°: Monthly Land-Surface
 666 Precipitation from Rain-Gauges built on GTS-based and Historic Data. DOI:
 667 [10.5676/DWD_GPCC/FD_M_V7_050](https://doi.org/10.5676/DWD_GPCC/FD_M_V7_050)
 668
 669 Skamarock, W.C., Klemp, J.B., Dudhia, J., Gill, D.O., Barker, D.M., Duda, M.G., Huang, X.Y.,
 670 Wang, W. and Powers, J.G., 2008. A description of the Advanced Research WRF version 3. NCAR
 671 Technical note-475+ STR, 113 pp.
 672
 673 Soleimani, Z., Parhizgari, N., Rad, H.D., Akhoond, M.R., Kermani, M., Marzouni, M.B., Goudarzi,
 674 H. and Goudarzi, G., 2015. Normal and dusty days comparison of culturable indoor airborne
 675 bacteria in Ahvaz, Iran. *Aerobiologia*, 31(2), pp.127-141.
 676
 677 Trigo, I.F., Bigg, G.R. and Davies, T.D., 2002. Climatology of cyclogenesis mechanisms in the
 678 Mediterranean. *Monthly Weather Review*, 130(3), pp.549-569.
 679
 680 Tropp, H. and Jagerskog, A., 2006. Water scarcity challenges in the Middle East and North Africa
 681 (MENA). *Human Development Paper. UNDP*. [http://hdr.undp.org/hdr2006/pdfs/background-](http://hdr.undp.org/hdr2006/pdfs/background-docs/Thematic_Papers/SIWI.pdf)
 682 [docs/Thematic_Papers/SIWI.pdf](http://hdr.undp.org/hdr2006/pdfs/background-docs/Thematic_Papers/SIWI.pdf).

683

684 Türkes, M., 1998. Influence of geopotential heights, cyclone frequency and Southern Oscillation
685 on rainfall variations in Turkey. *International Journal of Climatology*, 18(6), pp.649-680.

686

687 UN-ESCWA and BGR (United Nations Economic and Social Commission for Western Asia;
688 Bundesanstalt für Geowissenschaften und Rohstoffe). 2013. Inventory of Shared Water
689 Resources in Western Asia. Beirut.

690

691 Yu, Y., Notaro, M., Kalashnikova, O.V. and Garay, M.J., 2016. Climatology of summer Shamal
692 wind in the Middle East. *Journal of Geophysical Research: Atmospheres*.

693

694 Zaitchik, B.F., Evans, J.P., Geerken, R.A. and Smith, R.B., 2007a. Climate and vegetation in the
695 Middle East: interannual variability and drought feedbacks. *Journal of climate*, 20(15), pp.3924-
696 3941.

697

698 Zaitchik, B.F., Evans, J.P. and Smith, R.B., 2007b. Regional impact of an elevated heat source:
699 the Zagros Plateau of Iran. *Journal of Climate*, 20(16), pp.4133-4146.

700

701 Zarrin, A., Ghaemi, H., Azadi, M., Mofidi, A. and Mirzaei, E., 2011. The effect of the Zagros
702 Mountains on the formation and maintenance of the Iran Anticyclone using RegCM4.
703 *Meteorology and Atmospheric Physics*, 112(3-4), pp.91-100.

704

705 Zittis, G., Hadjinicolaou, P. and Lelieveld, J., 2014. Comparison of WRF Model Physics
706 Parameterizations over the MENA-CORDEX Domain. *American Journal of Climate Change*, 3(05),
707 p.490.
708

709 Table 1. Summary of the daily wind statistics over the region of the Zagros Barrier Jet (34.5-
710 35.5N, 43.5-45E). All the units are m/s. The first two rows include only days in the wet
711 composites and are for the total horizontal near-surface wind speed. Other rows incorporate
712 the entire period (1983-2013), and use only meridional component of the wind (925-850 hPa),
713 simulated by the WRF model.

	April	October
Mean WRF-wind speed in wet composite	7	6
Mean NCEP-wind speed in wet composite	2	1
Maximum WRF-meridional wind speed	20	16
Minimum WRF-meridional wind speed	-8	-10
Standard deviation of WRF-meridional wind speed	4.7	4.1
Mean of WRF-meridional wind speed	1.2	.3
90 th percentile of WRF-meridional wind speed	8.2	6.2
10 th percentile of WRF-meridional wind speed	-3.9	-4.1

714

Table 2. Coefficient of determination (R^2) between rainfall data and their components, when applicable, with the April Moisture Index (AMI) and the October Moisture Index (OMI). These indices are defined as the summation of standardized extreme vq values over the ZBJ region added to the standardized extreme uq values over the region representing the low-level westerly flow (39-41E, 36-40N). Values greater than the 80th percentiles are taken as extreme values. The R^2 values present the percentage of rainfall variability explained by these indices.

Rainfall data	AMI	OMI
GPCC	.48	.55
WRF/total	.46	.53
WRF/convective	.40	.51
WRF/non convective	.20	.11
NCEP/total	.06	.30
NCEP/convective	.03	.27
NCEP/non convective	.22	.06

723 Table 3. The contribution of ZBJ and LLW to the monthly rainfall totals in April and October. The
 724 WRF outputs are used to identify the days, analyzed in rows 2-4. Units in rows 1-5 are mm.
 725 Values in parentheses show the number of days used for their corresponding criteria. The last
 726 two rows show the RMSE and correlation coefficient between the GPCC monthly rainfall and
 727 the two models for the period 1983-2013.

	WRF/APR	NCEP/APR	WRF/OCT	NCEP/OCT
	(days)	(days)	(days)	(days)
Mean monthly	81.3 (930)	58.7 (930)	43.5 (961)	32.6 (961)
ZBJ >= 80 th percentile	38 (186)	26.4 (186)	24.5 (192)	17.3 (192)
LLW >= 80 th percentile	29.3 (186)	17.7 (186)	17.1 (192)	12.3 (192)
ZBJ >= 80 th or LLW >= 80 th percentile	54.4 (317)	36.7 (317)	31.2 (324)	21.7 (324)
Row 1 minus row 4	26.9	22	12.3	10.9
RMSE	20	40	13	19
Correlation coefficient	.84	.30	.85	.69

728

Figure captions:

Fig. 1 A: various components contributing to rainfall of the Tigris-Euphrates Headwaters (TEH), which is the region of interest in this study (black solid box). The arrows represent low-level flows affecting the rainfall of the TEH: Zagros Barrier Jet (ZBJ), Shamal winds, and low-level westerly (LLW) flow. The setup of the high (H) and low (L) pressure regions in this schematic resembles an active ZBJ and rainy day in the TEH. The favorable conditions for the Shamals are different (see the text). The green shading shows the Tigris-Euphrates Basin. The dashed black box is the WRF simulation domain. B: the topographic map of the domain. C: long-term mean (1988-2013) annual precipitation (mm/day) using GPCC daily data.

Fig. 2 A: annual cycle of total monthly rainfall (mm) for the GPCC, NCEP and WRF outputs, driven by NCEP boundary conditions (WRFN). B: annual cycle of the contribution of convective rainfall for the NCEP and WRFN. All are averaged over the TEH region (40-44E & 36-40N).

Fig. 3 A, D: long-term mean of observational precipitation (GPCC) patterns. B, E: time series of total monthly precipitation of GPCC, WRFN and NCEP over the period 1983-2013. C, F: histograms of daily precipitation events. The tail of the histograms has been trimmed to its 99th percentile for better presentation purposes. The time series and histograms are obtained from the regional means over the study area (40-44E & 36-40N). Upper and lower panels correspond to April and October, respectively.

751

752 Fig. 4 Comparing regionalization based on interannual variability of rainfall (1983-2013) using
753 GPCC, WRFN, and NCEP. Upper and lower panels correspond to April and October,
754 respectively. The black box shows the location of the study area.

755

756 Fig. 5 Composites of geopotential height (shading) and horizontal wind vectors using the
757 NCEP/DOE Reanalysis II data at 700 hPa. Wet (dry) composite includes days that the
758 WRF rainfall averaged over the TEH region, the red box, is greater (less) than its 90th
759 (10th) percentile over the period 1983-2013. Upper and lower panels correspond to April
760 and October, respectively.

761

762 Fig. 6 Horizontal near-surface wind, using WRF outputs and the NCEP data over the study
763 domain for the wet composite, which is the same as in Fig. 5. Shadings show the
764 patterns of the mean low-level geopotential heights (925-850 hPa). Upper and lower
765 panels correspond to April and October, respectively. The black box shows the location
766 of the TEH. The white areas in the left panels are regions with higher altitudes, and
767 therefore the surface pressure is lower than 850 hPa.

768

769 Fig. 7 The same as Fig. 6, but for the dry composite.

770

771 Fig. 8 Time series of daily (gray) and monthly mean (blue) meridional wind, v , averaged over a
772 region that represents the Zagros Barrier Jet (34.5-35.5N, 43.5-45E), for (A) April and (C)

October. B and D show the corresponding histograms of the daily time series. The 90th and 10th percentiles of daily data are also shown.

Fig. 9 A, B, D, E: Composites of near-surface horizontal moisture flux, using WRF outputs over the study domain, superimposed on the land surface topography (shading). Wet and dry composites are the same as in Fig. 5. Upper and lower panels correspond to April and October, respectively. The yellow and blue strips are used for vertical cross-section plots, shown in Figs. 10 and 12. The black box shows the location of the TEH region. C and F show the corresponding histograms of the daily meridional moisture flux, vq over the region that represents the Zagros Barrier Jet (34.5-35.5N, 43.5-45E), for April and October, respectively. The 90th and 10th percentiles of daily data are also shown.

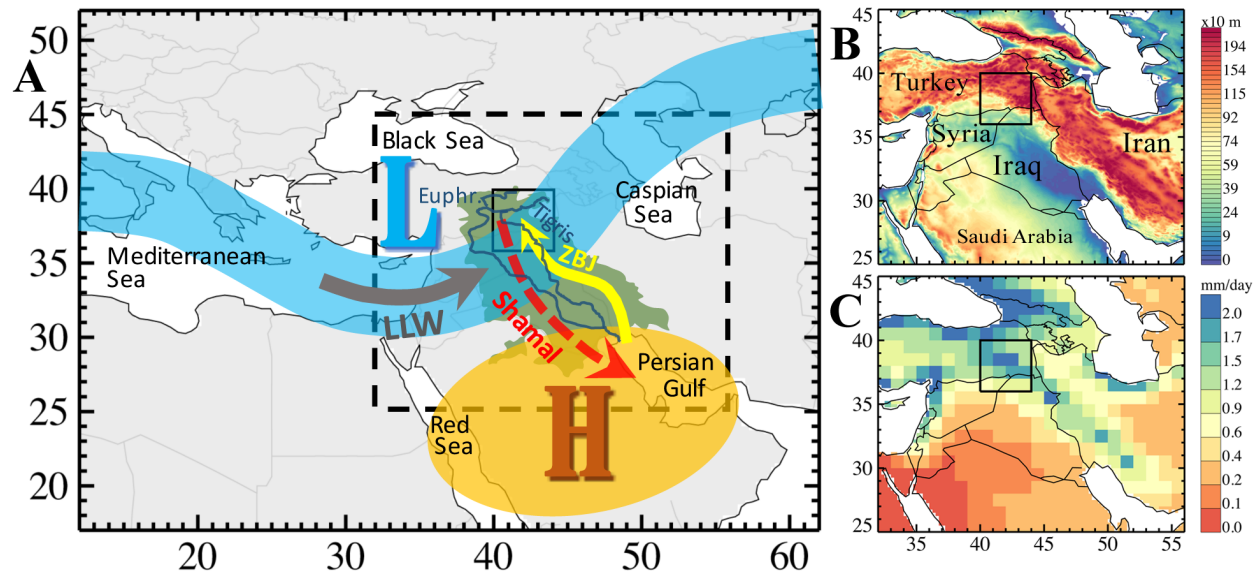
Fig. 10 Vertical cross-sections of meridional moisture flux, vq , averaged over the latitudes of the Zagros Barrier Jet (ZBJ), shown in Fig. 9 (the yellow strip). This plot is for the composite of high moisture flux (HMF) by the ZBJ. The HMF-ZBJ has been formed by compiling days with vq values higher than their 90th percentile, identified in Fig. 9c,f. The differences between WRF and NCEP vq below 700 hPa level and along the terrain are statistically significant at 1% level, using a Student's t-test.

Fig. 11 Spatial patterns of mean daily precipitation of WRF (left), NCEP (middle) and their difference (right) for the HMF-ZBJ composites, used in Fig. 10. Upper and lower panels

correspond to April and October, respectively. WRF-minus-NCEP precipitation values greater than 2.63 or less than -2.63 are significant at 1% level, using a Student's t-test.

Fig. 12 Spatial patterns of mean daily precipitation of WRF for the weak moisture flux (WMF-ZBJ) and moderate moisture flux (MMF-ZBJ) composites. Upper and lower panels correspond to April and October, respectively. These should be compared to HMF-ZBJ, shown in Fig. 11a,d.

Fig. 13 Vertical cross-section composites of zonal moisture flux, uq , along the blue strip, shown in Fig. 9. Composites consist of the days that WRF precipitation, averaged over the TEH region is greater than its 80th percentile and the NCEP precipitation is less than its median. The differences between WRF and NCEP uq below 700 hPa level and along the terrain are statistically significant at 1% level, using a Student's t-test.



809

810 Fig. 1 A: various components contributing to rainfall of the Tigris-Euphrates Headwaters (TEH),
 811 which is the region of interest in this study (black solid box). The arrows represent low-
 812 level flows affecting the rainfall of the TEH: Zagros Barrier Jet (ZBJ), Shamal winds, and
 813 low-level westerly (LLW) flow. The setup of the high (H) and low (L) pressure regions in
 814 this schematic resembles an active ZBJ and rainy day in the TEH. The favorable
 815 conditions for the Shamals are different (see the text). The green shading shows the
 816 Tigris-Euphrates Basin. The dashed black box is the WRF simulation domain. B: the
 817 topographic map of the domain. C: long-term mean (1988-2013) annual precipitation
 818 (mm/day) using GPCC daily data.

819

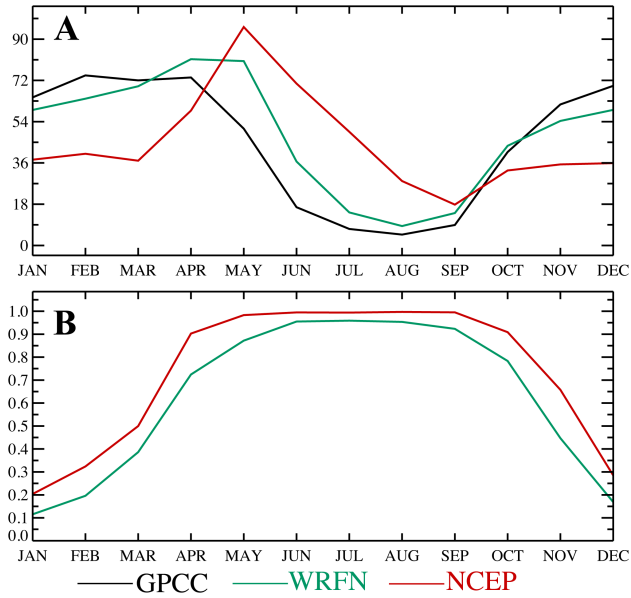


Fig. 2 A: annual cycle of total monthly rainfall (mm) for the GPCC, NCEP and WRF outputs, driven by NCEP boundary conditions (WRFN). B: annual cycle of the contribution of convective rainfall for the NCEP and WRFN. All are averaged over the TEH region (40-44E & 36-40N).

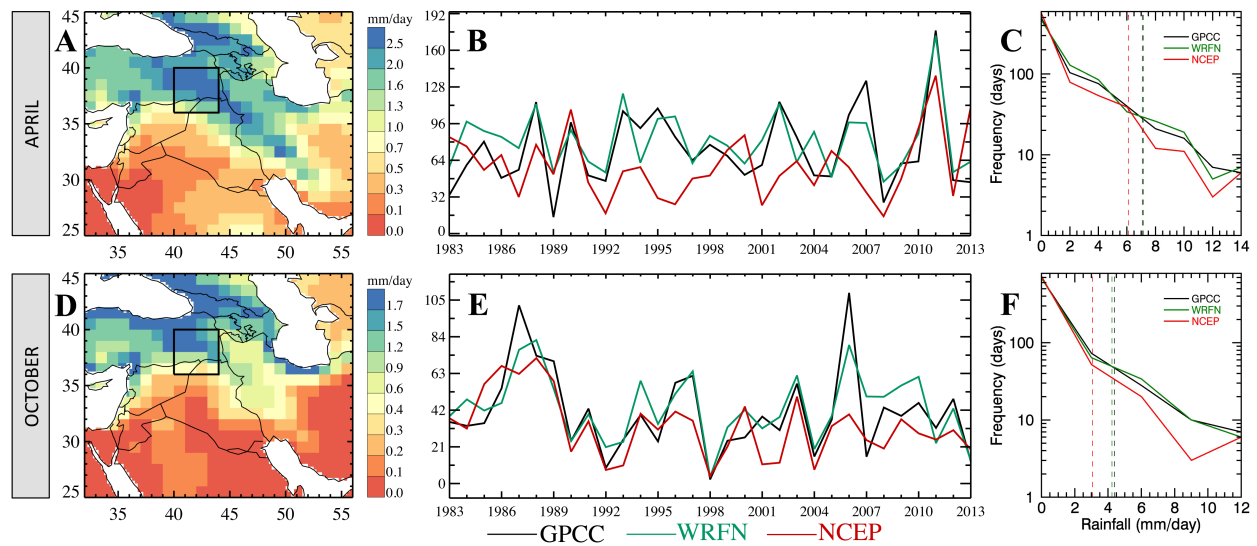


Fig. 3 A, D: long-term mean of observational precipitation (GPCC) patterns. B, E: time series of total monthly precipitation of GPCC, WRFN and NCEP over the period 1983-2013. C, F: histograms of daily precipitation events. The tail of the histograms has been trimmed to its 99th percentile for better presentation purposes. The time series and histograms are obtained from the regional means over the study area (40-44E & 36-40N). Upper and lower panels correspond to April and October, respectively.

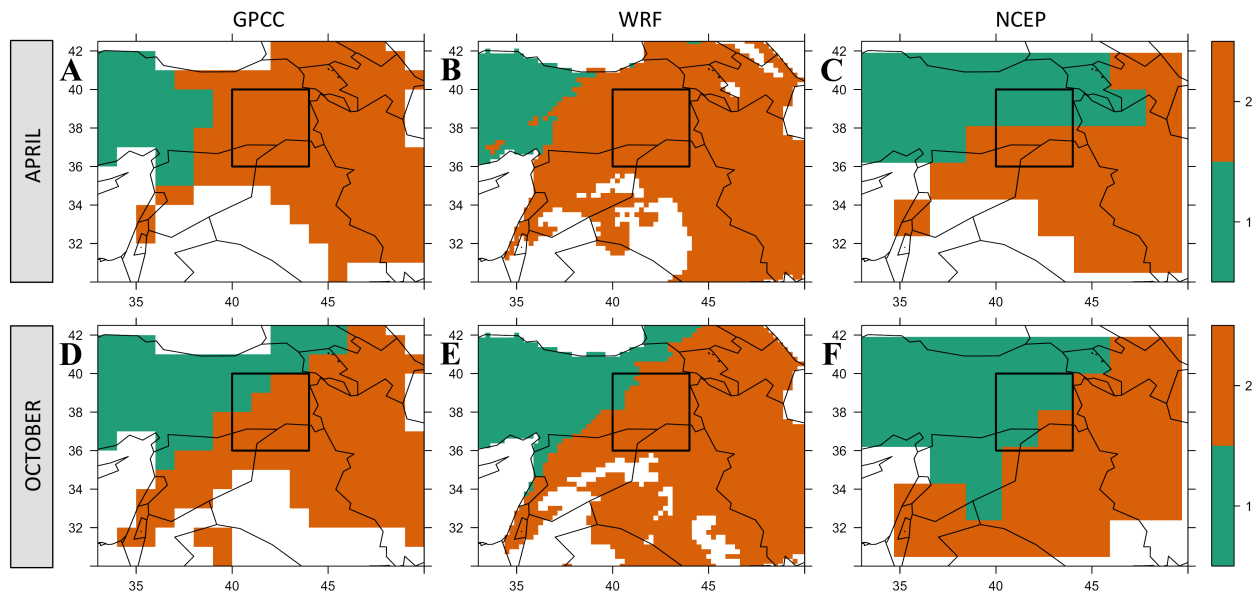


Fig. 4 Comparing regionalization based on interannual variability of rainfall (1983-2013) using GPCC, WRFN, and NCEP. Upper and lower panels correspond to April and October, respectively. The black box shows the location of the study area.

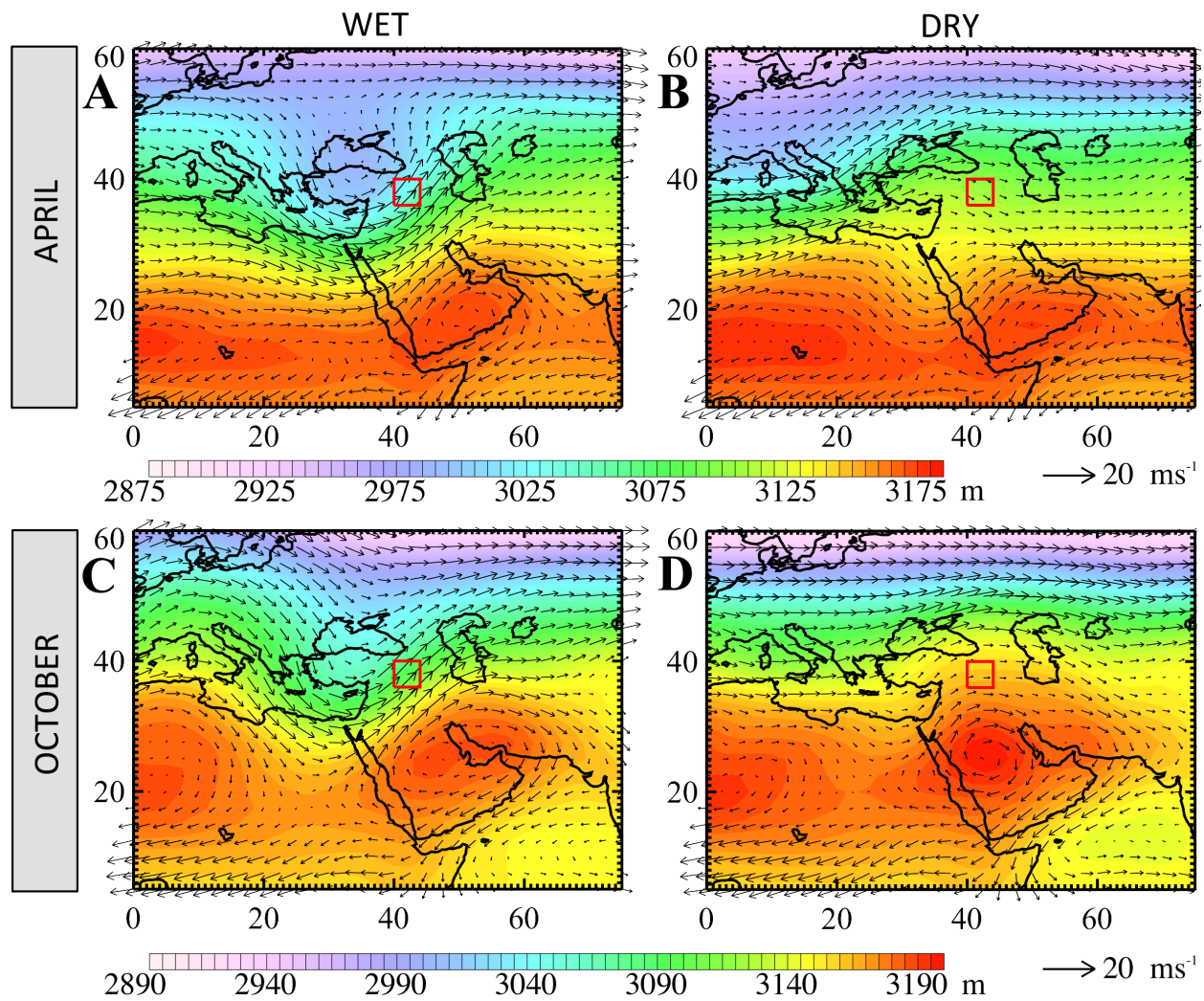


Fig. 5 Composites of geopotential height (shading) and horizontal wind vectors using the NCEP/DOE Reanalysis II data at 700 hPa. Wet (dry) composite includes days that the WRF rainfall averaged over the TEH region, the red box, is greater (less) than its 90th (10th) percentile over the period 1983-2013. Upper and lower panels correspond to April and October, respectively.

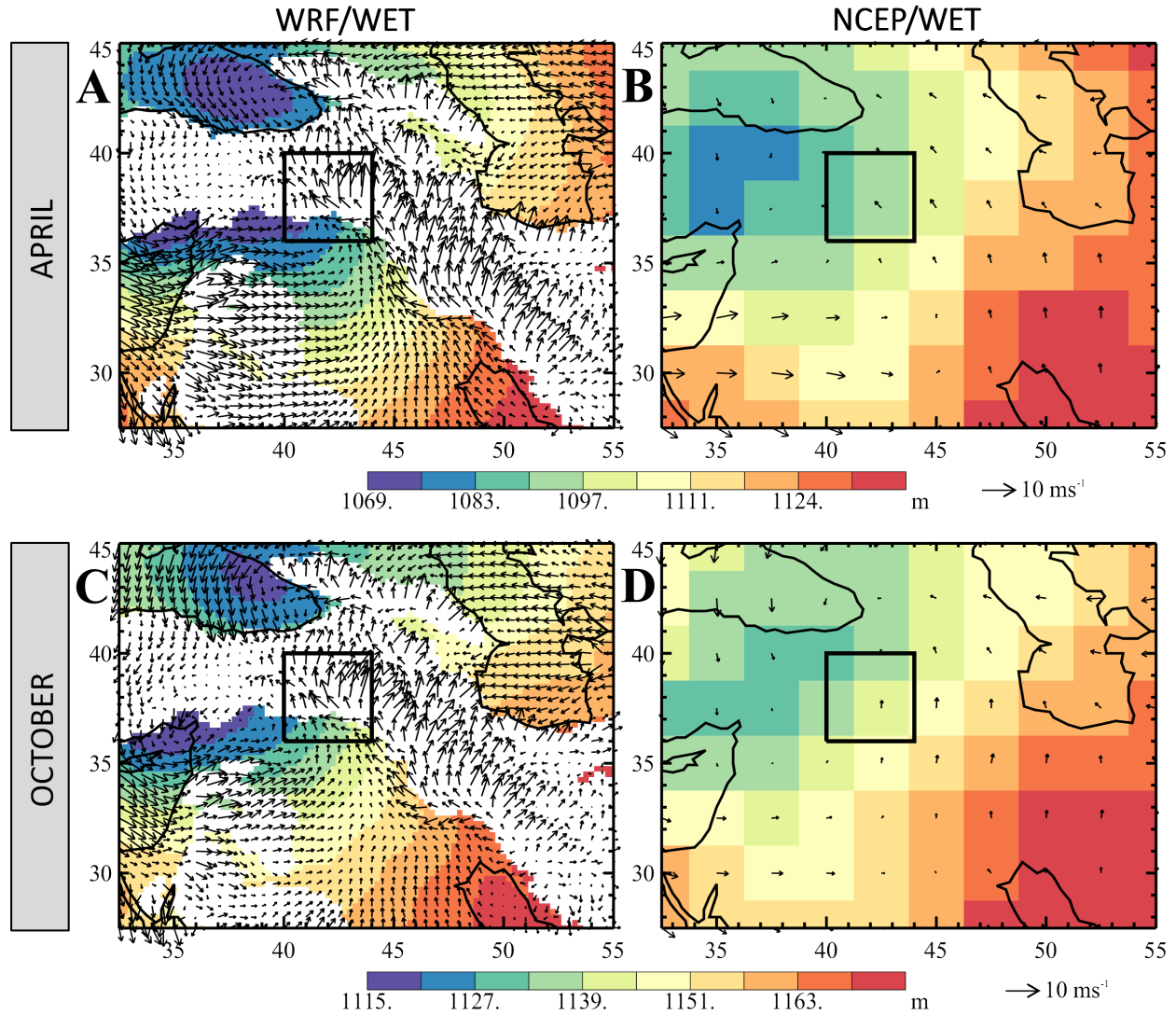


Fig. 6 Horizontal near-surface wind, using WRF outputs and the NCEP data over the study domain for the wet composite, which is the same as in Fig. 5. Shadings show the patterns of the mean low-level geopotential heights (925-850 hPa). Upper and lower panels correspond to April and October, respectively. The black box shows the location of the TEH. The white areas in the left panels are regions with higher altitudes, and therefore the surface pressure is lower than 850 hPa.

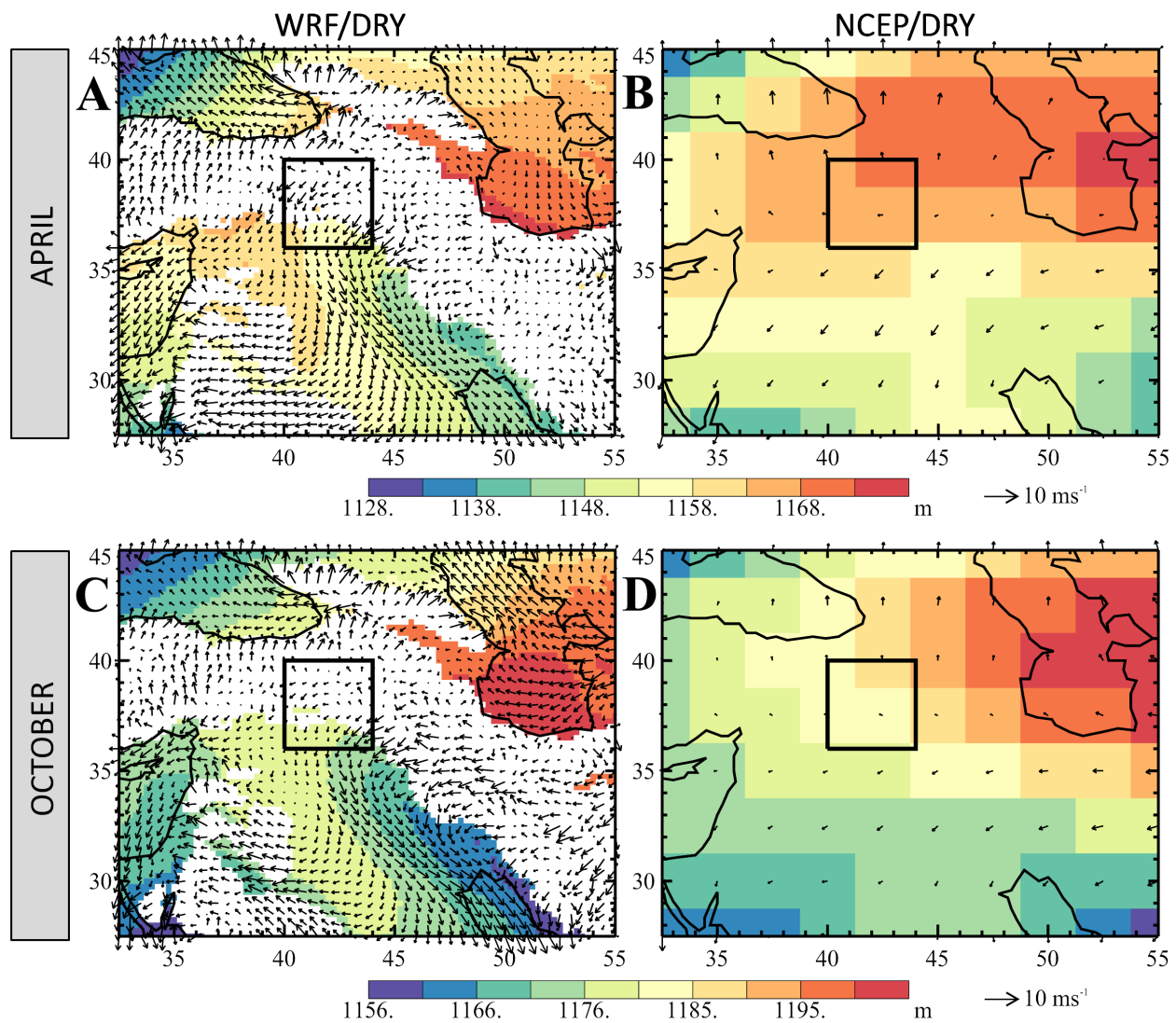


Fig. 7 The same as Fig. 6, but for the dry composite.

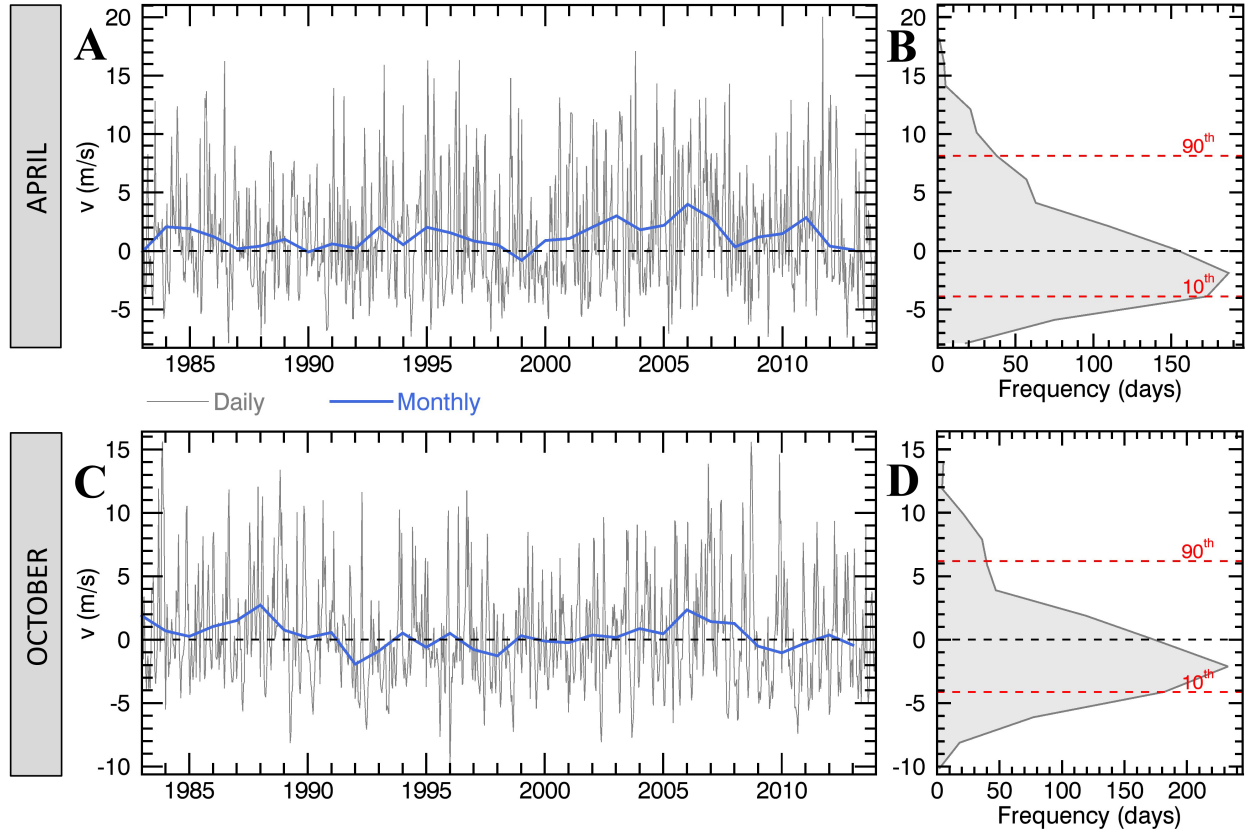


Fig. 8 Time series of daily (gray) and monthly mean (blue) meridional wind, v , averaged over a region that represents the Zagros Barrier Jet (34.5-35.5N, 43.5-45E), for (A) April and (C) October. B and D show the corresponding histograms of the daily time series. The 90th and 10th percentiles of daily data are also shown.

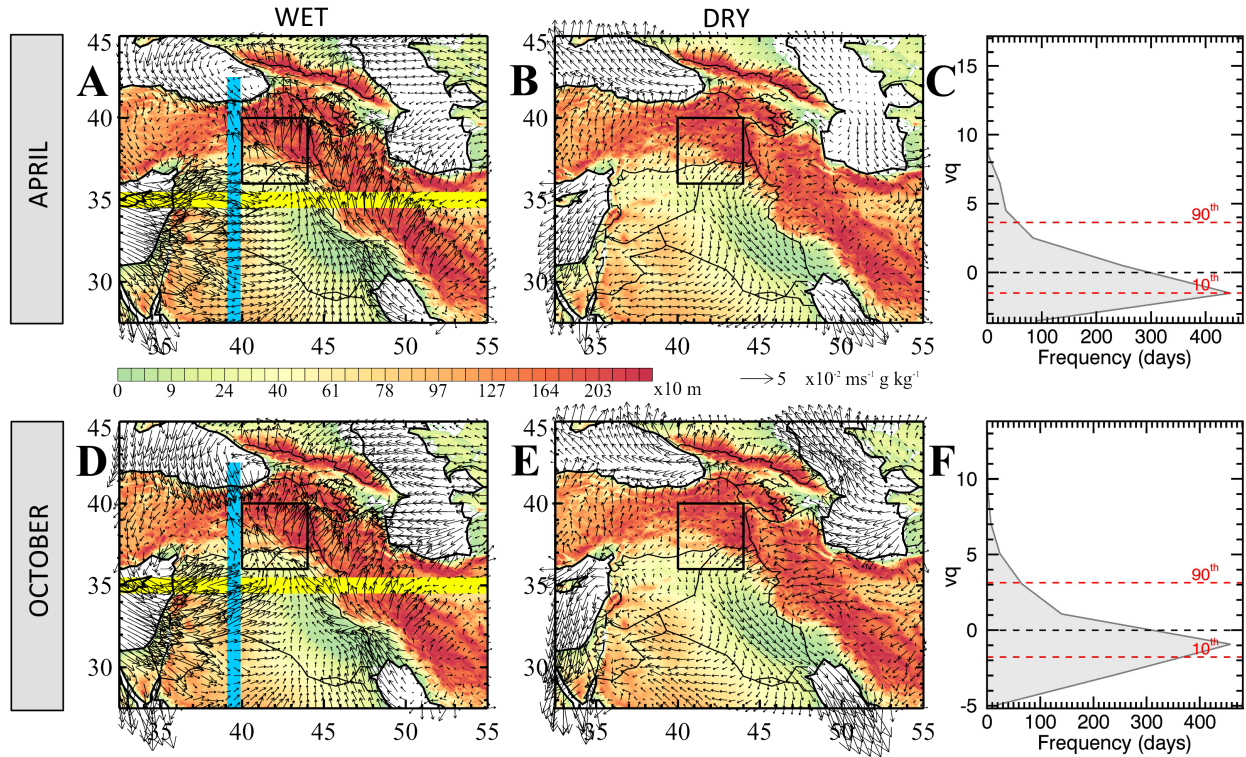


Fig. 9 A, B, D, E: Composites of near-surface horizontal moisture flux, using WRF outputs over the study domain, superimposed on the land surface topography (shading). Wet and dry composites are the same as in Fig. 5. Upper and lower panels correspond to April and October, respectively. The yellow and blue strips are used for vertical cross-section plots, shown in Figs. 10 and 12. The black box shows the location of the TEH region. C and F show the corresponding histograms of the daily meridional moisture flux, vq over the region that represents the Zagros Barrier Jet (34.5-35.5N, 43.5-45E), for April and October, respectively. The 90th and 10th percentiles of daily data are also shown.

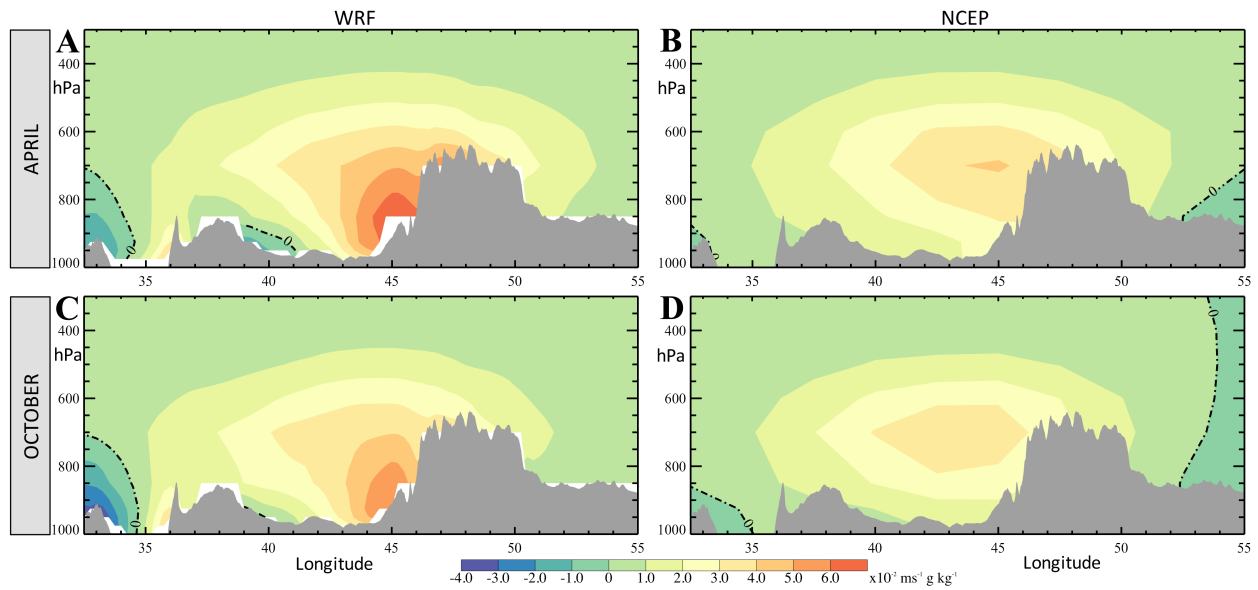


Fig. 10 Vertical cross-sections of meridional moisture flux, vq , averaged over the latitudes of the Zagros Barrier Jet (ZBJ), shown in Fig. 9 (the yellow strip). This plot is for the composite of high moisture flux (HMF) by the ZBJ. The HMF-ZBJ has been formed by compiling days with vq values higher than their 90th percentile, identified in Fig. 9c,f. The differences between WRF and NCEP vq below 700 hPa level and along the terrain are statistically significant at 1% level, using a Student's t-test.

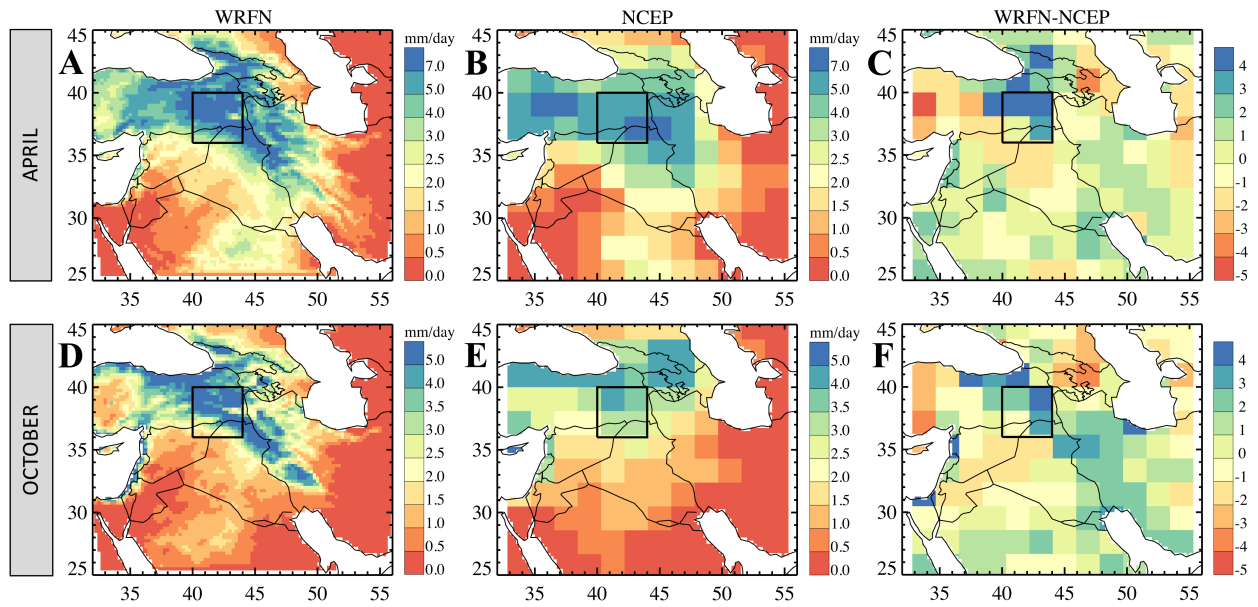


Fig. 11 Spatial patterns of mean daily precipitation of WRF (left), NCEP (middle) and their difference (right) for the HMF-ZBJ composites, used in Fig. 10. Upper and lower panels correspond to April and October, respectively. WRF-minus-NCEP precipitation values greater than 2.63 or less than -2.63 are significant at 1% level, using a Student's t-test.

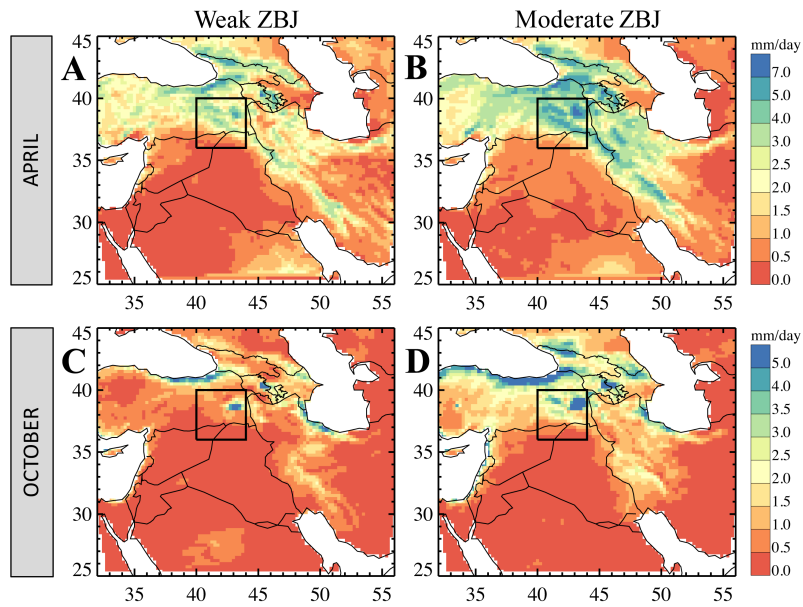


Fig. 12 Spatial patterns of mean daily precipitation of WRF for the weak moisture flux (WMF-ZBJ) and moderate moisture flux (MMF-ZBJ) composites. Upper and lower panels correspond to April and October, respectively. These should be compared to HMF-ZBJ, shown in Fig. 11a,d.

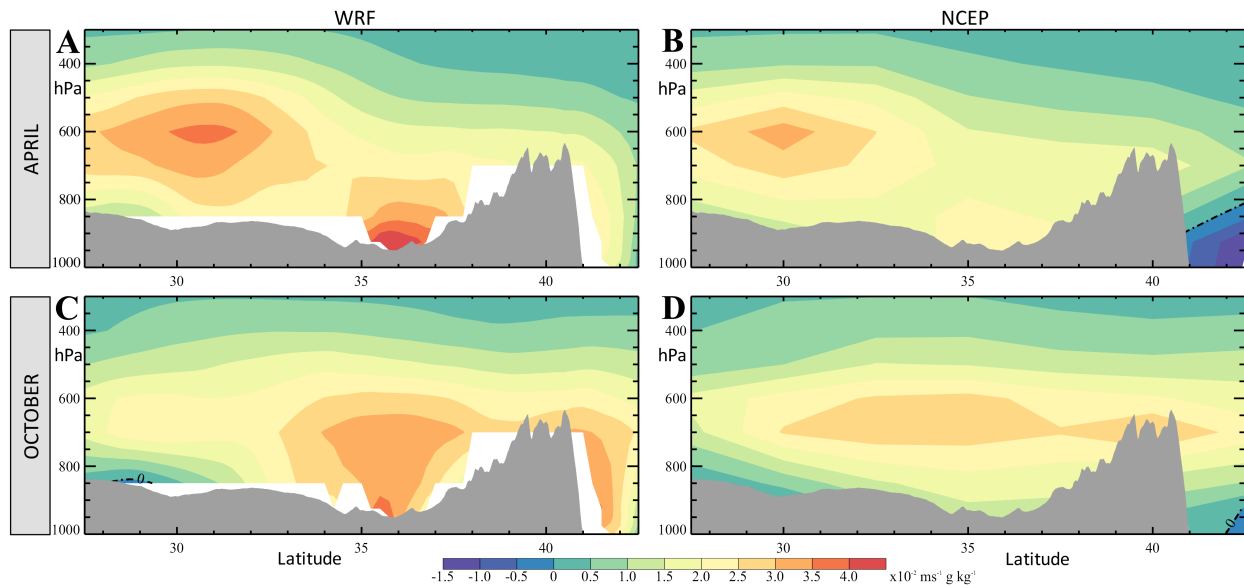


Fig. 13 Vertical cross-section composites of zonal moisture flux, uq , along the blue strip, shown in Fig. 9. Composites consist of the days that WRF precipitation, averaged over the TEH region is greater than its 80th percentile and the NCEP precipitation is less than its median. The differences between WRF and NCEP uq below 700 hPa level and along the terrain are statistically significant at 1% level, using a Student's t-test.